



Feasibility of ^{31}P spectroscopic imaging at 7 T in lung carcinoma patients

Quincy (.Q.). van Houtum¹  | Firdaus (.F.A.A.). Mohamed Hoesein¹ |
Joost (.J.J.C.). Verhoeff² | Peter (.P.S.N.). van Rossum² | Anne (.A.S.R.). van Lindert³ |
Tijl (.T.A.). van der Velden¹ | Wybe (.W.J.M.). van der Kemp¹ | Dennis (.D.W.J.). Klomp¹ |
Catalina (.C.S.). Arteaga de Castro¹ 

¹Radiology Department, University Medical Center Utrecht, Netherlands

²Radiotherapy Department, University Medical Center Utrecht, Netherlands

³Respiratory Medicine Department, University Medical Center Utrecht, Netherlands

Correspondence

Quincy van Houtum, MSc., University Medical Center Utrecht, Netherlands, Utrecht, Heidelberglaan 100, 3584 CX.
Email: qhoutum2@umcutrecht.nl, quincylvanhoutum@gmail.com

Currently, it is difficult to predict effective therapy response to molecular therapies for the treatment of lung cancer based solely on anatomical images. ^{31}P MR spectroscopic imaging could provide as a non-invasive method to monitor potential biomarkers for early therapy evaluation, a necessity to improve personalized care and reduce cost. However, surface coils limit the imaging volume in conventional ^{31}P MRSI. High-energetic adiabatic RF pulses are required to achieve flip angle homogeneity but lead to high SAR. Birdcage coils permit use of conventional amplitude modulated pulses, even over large FOV, potentially decreasing overall SAR massively. Here, we investigate the feasibility of 3D ^{31}P MRSI at 7 T in lung carcinoma patients using an integrated ^{31}P birdcage body coil in combination with either a dual-coil or a 16-channel receiver.

Simulations showed a maximum decrease in SNR per unit of time of 8% for flip angle deviations in short TR low flip-angle excitation 3D CSI. The minimal SNR loss allowed for fast 3D CSI without time-consuming calibration steps (>10:00 min.). ^{31}P spectra from four lung carcinoma patients were acquired within 29:00 minutes and with high SNR using both receivers. The latter allowed discrimination of individual phosphodiester, inorganic phosphate, phosphocreatine and ATP. The receiver array allowed for an increased FOV compared to the dual-coil receiver.

3D ^{31}P -CSI were acquired successfully in four lung carcinoma patients using the integrated ^{31}P body coil at ultra-high field. The increased spectral resolution at 7 T allowed differentiation of multiple ^{31}P metabolites related to phospholipid and energy metabolism. Simulations provide motivation to exclude ^{31}P B_1 calibrations, potentially decreasing total scan duration. Employing large receiver arrays improves the field of view allowing for full organ coverage. ^{31}P MRSI is feasible in lung carcinoma patients

Abbreviations: ^{31}P , Phosphorus; ATP, Adenosine triphosphate; CSI, Chemical Shift Imaging; FID, Free induction decay; GPC, Glycerophosphocholine; GPE, Glycerophosphoethanolamine; MRSI, Magnetic Resonance Spectroscopic Imaging; NADPH, Nicotinamide adenine dinucleotide phosphate; PC, Phosphocholine; PCr, Phosphocreatine; PDE, Phosphodiester; PE, Phosphoethanolamine; Pi, Inorganic Phosphate; PME, Phosphomonoesters; Rx, Receiver; SAR, specific absorption rate; TR, repetition time; UDPG, uridine diphosphoglucose

This is an open access article under the terms of the Creative Commons Attribution License, which permits use, distribution and reproduction in any medium, provided the original work is properly cited.

© 2019 The Authors. *NMR in Biomedicine* published by John Wiley & Sons Ltd

and has potential as a non-invasive method for monitoring personalized therapy response in lung tumors.

KEYWORDS

^{31}P MR spectroscopic imaging, *In vivo* application, lung carcinoma, response monitoring, X-nuclei MRS

1 | INTRODUCTION

In recent years, many new molecular therapies, such as immunotherapy, have been introduced for the treatment of lung cancer¹. Tumor cells generally use antigens to mask themselves from the immune system and immunotherapy exploits this mechanism by administering antibodies which specifically target tumor antigens. This labels the cell which allows it to be recognized by the own defense mechanisms of the body. The immune system responds by inhibiting or attacking the tumor cells, resulting in stalled tumor growth not necessarily accompanied by a decrease of tumor volume on imaging modalities².

Currently, it is difficult to predict which patients show an effective response to immunotherapy based on anatomical images like computed tomography only. Although a promising new treatment strategy for non-small cell lung carcinoma, immunotherapy is expensive and severe drug side effects are observed accompanied by an apparent decrease in quality of life. Therefore, there is an unmet need for a non-invasive method that can be used to predict tumor metabolic response which is crucial for early therapy effect evaluation. By adjusting the therapy strategy accordingly, such a tool would allow for more personalized curative care with less side effects, and reduced costs.

A recent study in breast cancer showed that changes in the phospholipid metabolism in responsive tumors can be detected after a single chemotherapy session using 31-phosphorous (^{31}P) magnetic resonance spectroscopic imaging (MRSI)^{3,4}. ^{31}P MRSI can detect the phospholipid and energy metabolites, which provides possibilities to monitor tissue metabolism non-invasively during treatment. Inorganic phosphate (Pi), phosphocreatine (PCr) and ATP (with the α -, β - and γ - resonances) allow assessment of the energy metabolism and the phosphomonoesters (PME) and phosphodiester (PDE) provide insight into the phospholipid metabolism⁴⁻⁷. Enhanced ratios of phosphocholine (PC) to glycerophosphocholine (GPC) and phosphoethanolamine (PE) to glycerophosphoethanolamine (GPE), are frequently observed in tumor tissue and correlated with proliferation⁷⁻¹². Another study in breast cancer demonstrated the feasibility of the phospholipid metabolism as biomarker for therapy follow-up and additionally reported shortening of the transverse relaxation time of Pi as a biomarker^{4,8,13}. As the physiological changes are present before any morphological changes have occurred, these metabolites, their ratios and individual MR properties are potential (bio-)markers for therapy response monitoring¹⁴⁻¹⁶.

However, the individual detection of ^{31}P metabolites is hampered at lower magnetic field strengths (3 T and below) due to the restricted spectral bandwidth and the low detection sensitivity. By going to higher magnetic field strengths (e.g. 7 T and higher), the SNR and spectral resolution are intrinsically enhanced^{17,18}. These properties have a tremendous advantage for the low abundant ^{31}P metabolites and even allow detection of the individual phosphomonoesters, (i.e. PE, PC) and diesters (i.e. GPE, GPC)¹⁹.

Unfortunately, the imaging volume in conventional ^{31}P MRSI is limited as small birdcage or surface coils are used^{5,20}. Surface coils generally require the use of high-energetic adiabatic RF pulses to achieve flip angle homogeneity as inhomogeneous excitations lead to signal variation in the acquired spectra over the large field of view. Adiabatic RF pulses usually result in high specific absorption rates (SAR), leading to longer repetition times (TR), clinically impractical scan times for a single protocol and a limiting number of consecutive scans. Full spectroscopic coverage of large organs such as the lungs is therefore challenging due to inhomogeneous $B_1^{+/-}$ fields and inhomogeneous excitation which increase with magnetic field strength.

In addition, MR imaging and spectroscopy are challenging near the lungs due to the presence of air, the relatively small amount of tissue and respiratory motion. Yet, previous studies claim that from a technical point of view MR imaging on clinical field strengths is a feasible method for screening lung cancer²¹.

Recent studies from Loring et al. and van Houtum et al. have presented a ^{31}P whole-body birdcage coil designed for 7 T^{22,23}. Using the body coil in combination with the conventional adiabatic pulses for high and low flip angle excitations requires adiabatic half passage or BIR4 pulses respectively and would increase the cost effective B_1^+ . This results in a narrow band width leading to multiple acquisition to capture the full spectra. By design this coil results in an improved homogeneous excitation, comparable to the ^1H whole-body birdcage coils of clinical 3 T MR systems. This allows the use of rectangular pulses, which decreases global and local SAR, creating opportunities for fast spectroscopic imaging methods. In addition, they demonstrated that this ^{31}P -body coil even allowed quantification of transverse relaxation times and the feasibility of obtaining high flip angle chemical shift imaging (CSI), over a large field of view. However, the use of this coil was revealed with a 30% inter-subject variation of the flip angle using a single power setting for multiple volunteers. This raises questions for the need for individual ^{31}P calibration, especially at low flip angles, as only the effective flip angle and not B_1^+ -field homogeneity is affected. Low flip angle excitations accompanied with short repetition

times (TR) can be used for fast 3D CSI. The optimal SNR per unit of time at lower flip angles is acquired when the Ernst angle (α_E) is used and any deviation from this flip angle result in additional T_1 weighting and a lower SNR per unit of time²⁴. The effects of a 30% flip angle deviation to the SNR per unit of time and consequently the acquired spectra can be evaluated by simulations. Excluding B_1 calibrations can decrease the total scan duration by 10 minutes or more, subsequently increasing patient comfort or allowing for additional scans or additional sampled averages to improve SNR.²⁵

The primary aim of this study was to investigate the feasibility of 3D ^{31}P MR spectroscopic imaging at ultra-high field in combination with a ^{31}P whole-body birdcage coil in four lung carcinomas.

2 | MATERIALS & METHODS

2.1 | Simulations

The effect of an uncalibrated excitation, that leads to a deviation from the Ernst angle (α_E) was assessed by simulating the SNR per unit of time for the α_E and for α_E with a $\pm 30\%$ and $\pm 50\%$ deviation over a TR/ T_1 -ratios range of 10^{-6} to 0.3. The latter is chosen with respect to a short TR of 60 ms and the longitudinal relaxation times (T_1) for ^{31}P metabolites of interest possibly ranging from 450 ms (α -ATP) to 7000 ms (GPE)⁶. The simulated spectroscopy signal shown in equation [1] was corrected for time differences by dividing with the square root of TR. The SNR per unit of time for all the calculated TR/ T_1 -ratios were normalized to the maximum signal at α_E .

$$\text{signal} \propto \frac{\sin(\alpha) \left(1 - e^{-\frac{TR}{T_1}}\right)}{1 - \cos(\alpha) e^{-\frac{TR}{T_1}}} \quad (1)$$

2.2 | Materials

^{31}P MRSI was performed using an in-house designed ^{31}P whole body birdcage coil integrated in a 7 T MR system (Philips Healthcare, Best, Netherlands)^{22,23}. The body coil, tuned at 120.6 MHz, was powered by a 25 kW amplifier (PID: 53-S26B-128, MKS Technologies, Shenzhen, Republic of China) resulting in a B_1^+ field-magnitude of $15\mu\text{T}$ at the isocentre. Two ^1H -TxRx/ ^{31}P -Rx arrays were constructed for the experiments. Array 1 (A1) contained a ^{31}P dual-coil receiver ($10 \times 16 \text{ cm}^2$, Figure 1A) and two fractionated ^1H dipole antennas (30 cm) used as transceivers, both driven in quadrature mode. Array 2 (A2) contained a 16-channel ^{31}P body array with eight integrated ^1H dipole antennas, shown in Figure 1B and C²⁶. Spectroscopic imaging data and anatomical proton images for localization were acquired in four patients using one of the two different setups.

2.3 | Patients & setup

Four stage III-IV non-small cell lung carcinoma patients (ages: 53–63 years; BMI: 17.7–29.5 Kg/m^2) were included in this feasibility study and signed informed consent prior to scanning. Two patients participated after their palliative chemo- and/or radiotherapy sessions and two patients

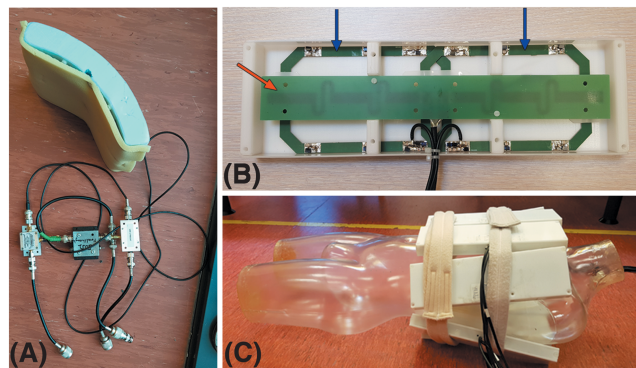


FIGURE 1 A.) image of the ^{31}P dual-coil receiver from A1 with an apparent curvature to allow close contact with the body. B.) a view of one of the eight elements of the ^{31}P 16-channel receiver array from A2. Two ^{31}P receiver coils, overlapped to improve decoupling, are denoted by blue arrows and the ^1H meander dipole antenna for MR imaging is shown by the red arrow. C.) all eight elements of the ^{31}P 16-channel receiver array positioned around a plastic human mannequin representable for the *in vivo* setup for MR spectroscopic imaging of the upper torso targeting the lungs

participated after the first immunotherapy cycle (see Table 1 for details). Patients were scanned in supine position. Scans of two patients were acquired with the ^{31}P dual coil Rx (A1) placed on the location closest to the tumor based on previously acquired clinical CT images for tumor localization. The other two patients were scanned with the ^{31}P Rx array (A2), that was wrapped around the upper part of their torso. The two separate dipole antennas in A1 are positioned on the side and the top of the lung of interest. Maximum tumor dimension ranged from 25 mm to 75 mm and other clinical details per patient are shown in Table 1.

2.4 | MR data acquisition

No B_0 shimming was performed nor was the ^{31}P B_1^+ calibration. Phosphorus (^{31}P) spectra were acquired using a 3D ^{31}P acquisition weighted CSI protocol including elliptical k-space sampling. Excitation was performed using rectangular RF pulses only and the carrier frequency was set to PCR. The isotropic resolution ranged from 20 to 30 mm and other parameters are summarized in Table 2²⁴.

2.5 | Data processing

Spectroscopic data from the 3D CSI protocol were processed in Matlab 2018b (The Mathworks Inc., Natick, MA) using an open source in-house designed processing tool (CSlgui v1.1, <http://www.csigui.tk>, April 2019). ^{31}P spectroscopy data were averaged and spatially filtered using a 3D hamming window followed by an inverse Fourier transformation to the spatial domain. All free induction decays (FID) were apodized using a 24 Hz gaussian filter and zero filled to 512 samples. Coil data was combined using the whitened singular value decomposition (WSVD) algorithm as reported by Rodgers et al²⁷. Zeroth order phase correction was applied automatically, and first order phase correction was applied manually, thereafter. No additional nor aesthetic baseline corrections were performed. Spectra from tumors exceeding the voxel resolution were aligned to the metabolite peak with the highest SNR followed by averaging, excluding voxels with a 50% or less partial tumor tissue volume on available MR images. The SNR of metabolites was calculated using equation [2] with S_{max} , the real part of the maximum signal intensity and the noise defined as the absolute standard deviation of the last 50 samples points of the spectrum.

$$\text{SNR} = \frac{\text{real}(S_{\text{Max}})}{|\text{std}(S_{\text{noise}})|} \quad (2)$$

TABLE 1 Clinical details of each patient including relevant remarks. The body-mass-index (BMI) is calculated as the weight (kg) divided by the length squared (m^2). Tumor sizes (cm^3) represent the maximum tumor length in each direction (RL x AP x FH) and corresponding maximum volumes (cc) determined from MR and/or CT images. Treatment of non-small cell lung carcinoma for these patients included systemic body radiation therapy (SBRT), chemoradiation and immunotherapy (Erlotinib, Pembrolizumab abbreviations: Superior vena cava (SVC))

Patient	Age (years)	BMI (kg/m^2)	Tumor size (cm^3)[cc]	Therapy	Remarks
#1	59	20.4	7.25 x 1.75 x 1.00 12.69	Seq. Chemoradiation	Stent in SVC close to tumor
#2	60	17.7	3.75 x 4.80 x 2.00 36.00	Thoracic SBRT	-
#3	63	24.2	3.60 x 3.20 x 3.60 41.47	Erlotinib	-
#4	53	29.5	3.60 x 3.00 x 2.50 27.00	Pembrolizumab	-

TABLE 2 3D ^{31}P CSI protocol parameters for each patient including the resolution, matrix size (RL x AP x FH), repetition time (TR), echo time (TE), flip angle, bandwidth (BW), number of sampled averages (NSA), number of sample points, scan duration and number of ^{31}P receiver channels (#Rx). α nominal voxel volume corrected for weighted acquisition²⁴

Patient	Resolution nominal (mm^3) real (cc) ^{α}	Matrix (RL x AP x FH)	TR/TE (ms)	Flip angle	BW (Hz)	NSA	Sample points	Scan duration (min: Sec)	#Rx (^{31}P)
#1	26 x 26 x 26 31	7 x 5 x 6	60/0.54	20°	4800	320	256	23:00	2
#2	20 x 20 x 20 14	12 x 7 x 9	60/0.54	12°	4800	80	256	23:00	2
#3	30 x 30 x 30 48	12 x 6 x 6	60/0.51	9°	5000	60	256	25:55	16
#4	30 x 30 x 30 48	15 x 11 x 8	60/0.44	10°	4800	60	256	28:15	16

3 | RESULTS

Simulations resulted in a maximum decrease of 8% in SNR per unit of time within the used TR/T₁ range for + and - 30% deviating flip angles, as can be seen in Figure 2. In addition, the $\alpha_E + 30\%$ variation showed a lower decrease in SNR per unit of time compared to the $\alpha_E - 30\%$ variation. A similar trend is seen for a $\alpha_E \pm 50\%$ variation showing a maximum decrease of 23% in SNR per unit of time within the same TR/T₁ range for the $\alpha - 50\%$ variation. According to the B₁ maps available for the ³¹P body coil, we could expect a maximum of 30% deviation in flip angle in the *in-vivo* measurements using equal power settings between subjects and, in addition, a maximum decrease in SNR per unit of time of less than 6% is seen for the TR/T₁-ratios range that corresponds to the ³¹P metabolites of interest (0.009; 0.13) and the proposed protocol TR (60 ms)²³.

All patients were imaged within an hour of scan time with one of the two setups. Positioning the ¹H transmit coils for patient #1 was limited due to a stent in the superior vena cava (SVC) located close to the tumor. No other patient related difficulties were experienced during the scan sessions. Images obtained with the dipole antenna in A1 were adequate for tumor localization and planning (Figure 3A), when tumor location was known from previous CT images (Figure 3B).

Images and tumor localization using A2 were improved compared to A1 as is depicted in Figure 3A and 3E. Spectroscopic imaging acquisitions could be obtained with both setups as shown in figures 3C & E, where a single spectroscopy slice from the 3D imaging set for patient #1 and #4 are shown respectively. Tumor voxels in the slice used for averaging are marked by the red and yellow rectangles, showing 8 out of 20 voxels for patient #1 and all tumor voxels for patient #4. In addition, the signal intensity of the voxels located at the posterior side of the patient in the spectroscopic imaging array in Figure 3E have higher SNR compared to the anterior side.

Obtained ³¹P lung carcinoma spectra were acquired with high SNR for PCr (9.5) and the ATP resonances (>4.7) using A1, the ³¹P dual-coil Rx (Figure 4A) and with high SNR ranging from 3.9 (PME) to 13.2 (α -ATP) using A2, the ³¹P 16-channel Rx array (Figure 4B). It allowed discrimination of PME, Pi, PDE, PCr in all patients, the three ATP resonances and UDPG in all subjects except for patient #1 and NADPH in patient #4. Moreover, the SNR of the phospholipid- and energy- metabolites was found higher with A2 compared to A1. The lack of B₀ shimming and partial volume effects over the large field of view is visible in the spectra with measured linewidths ranging from 0.20 ppm to 1.1 ppm after apodization when using either coil setup.

4 | DISCUSSION

3D ³¹P spectroscopic imaging was successfully obtained in four lung carcinoma patients with either the ³¹P dual-coil receiver or the 16-channel receiver array in combination with the integrated ³¹P body coil at 7 tesla. Both Rx setups allowed the acquisition of phosphorous metabolic information from the lung carcinoma via a non-invasive method, while targeting the full organ for evaluation. The increased spectral resolution at the ultra-high magnetic field strength of 7 T allowed differentiation of multiple phosphorous metabolites related to cell membrane and energy metabolism. A minimal decrease in SNR per unit of time was apparent from the simulations performed to study the effect of a +/-30% deviation from the Ernst angle due to the lack of individual body coil power calibrations in this patient population. This minimal SNR loss of at maximum 8% allowed for 3D fast spectroscopic imaging with short TR and low flip angle excitation without time-consuming calibration steps during the scan session.

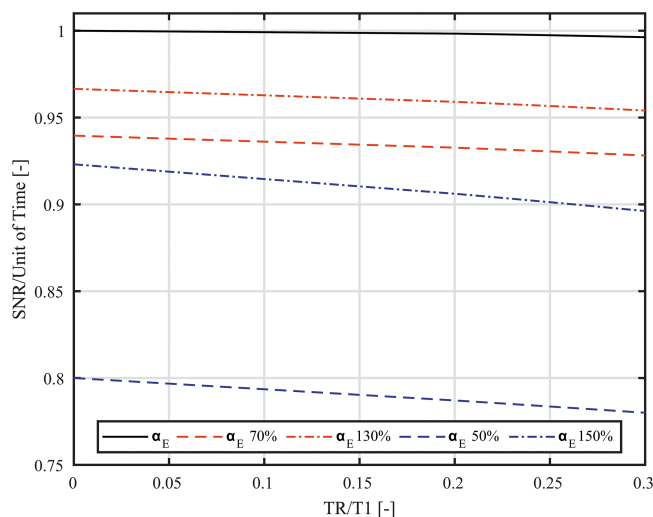


FIGURE 2 Simulation of the SNR per unit of time for the 3D ³¹P spectroscopic imaging at Ernst angle (α_E) and with a 30% and 50% deviation for the TR/T₁ ratio ranging from 10⁻⁶ to 0.3. The SNR per unit of time at α_E is marked by the solid black line, the increased and decreased angles for both the 30% (red) and 50% (blue) deviations are displayed as dashed and dash-dotted lines respectively

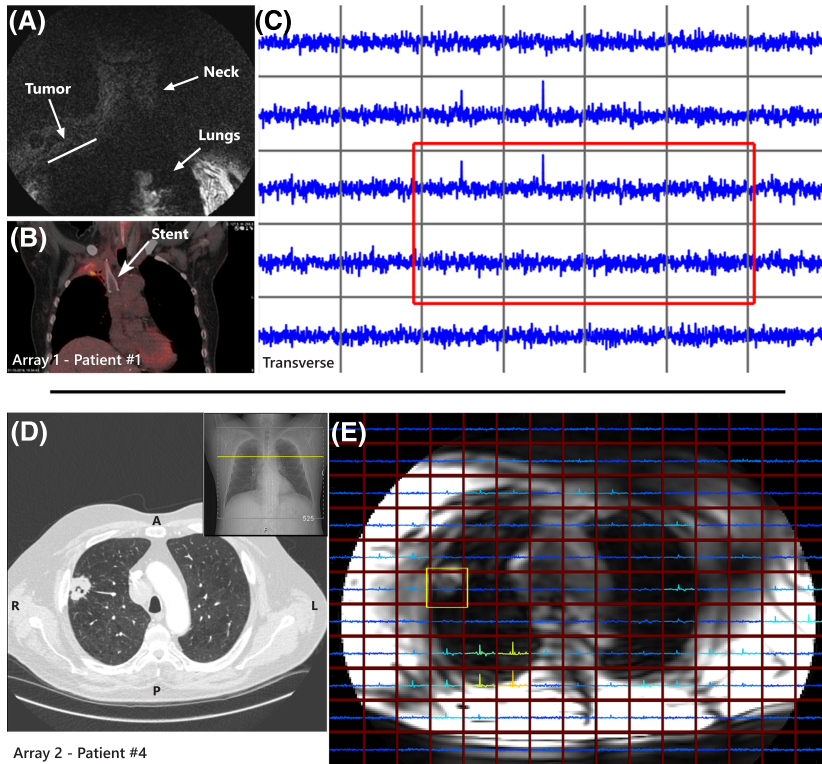


FIGURE 3 A) Coronal MR image including labels for the tumor, neck and lungs plus B) a coronal CT image with PET scan overlay, both from patient #1 and used for tumor localization. C) Single transverse slice of the 3D spectroscopic imaging data from patient #1 with the tumor voxels indicated by the red rectangle. D) Transverse and coronal CT images from patient #4 for tumor localization and planning. E) the MR image from patient #4 with an overlay of a single slice of the 3D spectroscopic imaging data. Tumor voxel is highlighted by the yellow rectangle

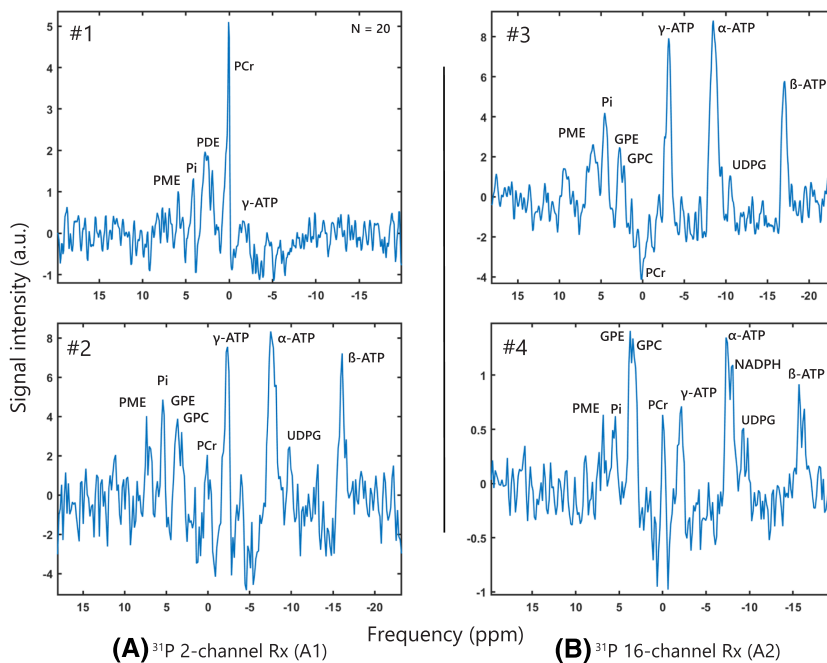


FIGURE 4 Spectra of lung tumor tissue for all four patients acquired with the ^{31}P chemical shift imaging protocol using a) A1, the ^{31}P dual coil Rx and B) A2, the ^{31}P 16-channel Rx array. Phosphomonoesters (PME), phosphodiester (PDE), glycerophosphoethanolamine (GPE) plus glycerophosphocholine (GPC), inorganic phosphate (pi), phosphocreatine (PCr) and the α -, β - and γ -ATP resonances are labelled where applicable. The number of tumor voxels used for averaging is denoted by N in the right top corner of the spectrum except for single voxel spectra. Notice the increase in PDE with respect to PME in patient #4 that might indicate tumor response to immunotherapy

Increasing the number of receiver coils improved the field of view coverage of ^{31}P MRS images expanding the available metabolic information over a larger field of view. This agrees with previous demonstrations in literature²⁸. In addition, the SNR increase gained with the 16-channel receiver array used in patient #3 and #4 not only allowed discrimination of PME, Pi, GPE, GPC, PCr, ATP (with α -, β - & γ -resonances) and uridine-diphosphate glucose (UDPG) as with the dual-coil receiver but also nicotinamide-adenine dinucleotide phosphate (NADPH) in patient #4. UDPG is a known liver metabolite and indicates minor liver signal contamination, however SNR was insignificant ($\text{SNR} < 3$)⁵. NADPH ($\text{SNR} > 3$) however, though also found in the liver, is a cofactor involved with anabolic reactions, already linked to tumor tissue²⁹. In addition, the highest SNR of the dual-coil receiver was measured for PCr (Figure 4A, Patient #1) which is not directly associated with tumor tissue, but rather muscle tissue⁵. This can be explained by signal contamination from chest muscle signals contained in neighbouring voxels that bled in the tumor

voxel location due to the small field of view of this patient, which excluded the full body circumference, in combination with the relatively large voxel size. Additional averaging of the 20 voxels also increased signal contamination in this patient but was required to regain the SNR of the spectrum. Spectra acquired with the 16ch Rx still show signal contamination, as can be seen by the remaining PCr peaks, though to a lesser extent than the first patient and even in opposite phase (Figure 4B, patient #3). The lung and tumor morphology itself may already minimize signal contamination from neighboring voxels as tissue density in healthy lung tissue is, compared to other areas in the body, extremely low. Further protocol development could minimize signal contamination within a short time frame by increasing spatial voxel resolution or reducing point spread by more complex k-space weightings and filtering²⁴. Another strategy could be the use of selective pulses to fully eliminate specific tissue signal such as the one coming from the muscles.

The top part of the torso, especially at the collar bones, limits proper positioning of the top elements of the receiver array. The eight rigid elements of the array lack the body-shaped curvature, disfavoring coil loading and resulting in a suboptimal receive fields for these coils. This can be seen by the increased SNR at the posterior side of the patient compared to the anterior voxels shown in Figure 3C. Additional suboptimal coil combinations using the WSVD algorithm could also disfavor the SNR gradient over the spectroscopic image.

Moreover, in the presence of large susceptibility differences, such as the lung itself, implants and the moving heart, spectral quality is surprisingly adequate for the distinction of the metabolites, even without B_0 shimming. Resulting B_0 homogeneity was adequate with a spectral linewidth ranging between 0.2 and 1.1 ppm. This B_0 non-uniformity is much less critical than for ^1H MRS as the spectral separation between metabolites (i.e. PME versus PDE) is substantial (i.e. >3.5 ppm) at 7 T. However, it should still be noted that the B_0 field uniformity can be highly variable both spatially as temporally. In our previous study we simulated spatiotemporal magnetic field uniformity, which at worst case conditions (i.e. at diaphragm comparing fully inhaled versus exhaled condition) could be up to 3 ppm³⁰. Either avoiding inclusion of subjects with tumors in locations of such severe non uniformities or using new means of local shim coils that can mitigate these distortions may be required³¹. In addition, shimming procedures could be performed within a breath-hold and when combined with gating it is expected to improve linewidth, possibly increasing sensitivity to allow detections of the individual PME and PDE³².

In this study we have altered the flip angle between subjects. As prior knowledge about signal levels was unknown, we started by focusing on ATP, therefore setting the flip angle to 20° . After confirming observation of phospholipids, the angle was set to 9° (i.e. Ernst angle for PME and PDE). Finally, we completed the protocol by small over-tipping to also consider SNR of other metabolites that all have a shorter T_1 . Note that the spectra are obtained with T_1 weighting, so altered peak ratios can be caused by concentration differences, but also by alterations in T_1 . To extract the T_1 dependence, subject specific T_1 knowledge could be obtained by acquiring the same scan twice albeit with a different flip angle.

5 | CONCLUSION

We conclude that ^{31}P MRSI in lung carcinoma is feasible at 7 T. Employing large receiver arrays that can cover the whole torso, improves the field of view coverage allowing full organ ^{31}P -MRSI acquisition. With only minor signal contamination to overcome, ^{31}P MRSI shows great potential as tumor biomarker for treatment response monitoring in lung cancer.

ORCID

Quincy (Q.). van Houtum  <https://orcid.org/0000-0002-6690-1018>

Catalina (C.S.). Arteaga de Castro  <https://orcid.org/0000-0002-1055-2672>

REFERENCES

1. Hirsch FR, Scagliotti GV, Mulshine JL, et al. Lung cancer: current therapies and new targeted treatments. *Lancet*. 2017;389(10066):299-311. [https://doi.org/10.1016/S0140-6736\(16\)30958-8](https://doi.org/10.1016/S0140-6736(16)30958-8)
2. Ribas A, Wolchok JD. Cancer immunotherapy using checkpoint blockade. *Science*. 2018;359(6382):1350-1355. <https://doi.org/10.1126/science.aar4060>
3. Krikken E, van der Kemp WJM, van Diest PJ, et al. Early detection of changes in phospholipid metabolism during neoadjuvant chemotherapy in breast cancer patients using phosphorus magnetic resonance spectroscopy at 7T. *NMR Biomed*. 2019;32(6):e4086. <https://doi.org/10.1002/nbm.4086>
4. van der Kemp WJ, Stehouwer BL, Luijten PR, van den Bosch MA, Klomp DW. Detection of alterations in membrane metabolism during neoadjuvant chemotherapy in patients with breast cancer using phosphorus magnetic resonance spectroscopy at 7 tesla. *Springerplus*. 2014;3. <https://doi.org/10.1186/2193-1801-3-634>
5. Valkovič L, Chmelík M, Krššák M. In-vivo ^{31}P -MRS of skeletal muscle and liver: a way for non-invasive assessment of their metabolism. *Anal Biochem*. 2017;529:193-215. <https://doi.org/10.1016/j.ab.2017.01.018>
6. Chmelík M, Považan M, Krššák M, et al. In vivo ^{31}P magnetic resonance spectroscopy of the human liver at 7 T: an initial experience. *NMR Biomed*. 2014;27(4):478-485. <https://doi.org/10.1002/nbm.3084>
7. Klomp DWJ, van de Bank BL, Raaijmakers A, et al. ^{31}P MRSI and ^1H MRS at 7 T: initial results in human breast cancer. *NMR Biomed*. 2011;24(10):1337-1342. <https://doi.org/10.1002/nbm.1696>

8. van der Kemp WJM, Boer VO, Luijten PR, Stehouwer BL, Veldhuis WB, Klomp DWJ. Adiabatic multi-echo ^{31}P spectroscopic imaging (AMESING) at 7 T for the measurement of transverse relaxation times and regaining of sensitivity in tissues with short T_2^* values. *NMR Biomed*. 2013;26(10):1299-1307. <https://doi.org/10.1002/nbm.2952>
9. Negendank W. Studies of human tumors by MRS: a review. *NMR Biomed*. 1992;5(5):303-324. <https://doi.org/10.1002/nbm.1940050518>
10. Glunde K, Jie C, Bhujwalla ZM. Molecular causes of the aberrant choline phospholipid metabolism in breast Cancer. *Cancer Res*. 2004;64(12):4270-4276. <https://doi.org/10.1158/0008-5472.CAN-03-3829>
11. Park JM, Park JH. Human in-vivo ^{31}P MR spectroscopy of benign and malignant breast tumors. *Korean J Radiol*. 2001;2(2):80-86. <https://doi.org/10.3348/kjr.2001.2.2.80>
12. Runge JH, van der Kemp WJM, Klomp DWJ, Luijten PR, Nederveen AJ, Stoker J. 2D AMESING multi-echo ^{31}P -MRSI of the liver at 7T allows transverse relaxation assessment and T_2 -weighted averaging for improved SNR. *Magn Reson Imaging*. 2016;34(2):219-226. <https://doi.org/10.1016/j.mri.2015.10.018>
13. van der Kemp WJM, van der Velden TA, Schmitz AM, et al. Shortening of Apparent Transverse Relaxation Time of Inorganic Phosphate as a Breast Cancer Biomarker. *NMR Biomed*. 2018. <https://doi.org/10.1002/nbm.4011>
14. Steen RG. Response of solid tumors to chemotherapy monitored by in vivo ^{31}P nuclear magnetic resonance spectroscopy: a review. *Cancer Res*. August 1989;49(15):4075-4085.
15. Ng TC, Grundfest S, Vijayakumar S, et al. Therapeutic response of breast carcinoma monitored by ^{31}P MRS in situ. *Magn Reson Med*. 1989;10(1):125-134. <https://doi.org/10.1002/mrm.1910100112>
16. Semmler W, Gademann G, Bachert-Baumann P, Zabel HJ, Lorenz WJ, van Kaick G. Monitoring human tumor response to therapy by means of P-31 MR spectroscopy. *Radiology* 1988;166(2):533-539. <https://doi.org/10.1148/radiology.166.2.3336731>
17. Kraff O, Fischer A, Nagel AM, Mönninghoff C, Ladd ME. MRI at 7 tesla and above: demonstrated and potential capabilities. *J Magn Reson Imaging*. 2015;41(1):13-33. <https://doi.org/10.1002/jmri.24573>
18. Redpath TW. Signal-to-noise ratio in MRI. *BJR*. 1998;71(847):704-707. <https://doi.org/10.1259/bjr.71.847.9771379>
19. Purvis LAB, Clarke WT, Valkovič L, et al. Phosphodiester content measured in human liver by in vivo ^{31}P MR spectroscopy at 7 tesla. *Magn Reson Med*. 2017;78(6):2095-2105. <https://doi.org/10.1002/mrm.26635>
20. van der Kemp WJM, Klomp DWJ, Wijnen JP. ^{31}P T_2 s of phosphomonoesters, phosphodiesters, and inorganic phosphate in the human brain at 7T. *Magn Reson Med*. 2018;80(1):29-35. <https://doi.org/10.1002/mrm.27026>
21. Biederer J, Ohno Y, Hatabu H, et al. Screening for lung cancer: does MRI have a role? *Eur J Radiol*. 2017;86:353-360. <https://doi.org/10.1016/j.ejrad.2016.09.016>
22. Löring J, van der Kemp WJM, Almujaayaz S, van Oorschot JWM, Luijten PR, Klomp DWJ. Whole-body radiofrequency coil for (^{31}P) P MRSI at 7T. *NMR Biomed*. 2016;29(6):709-720. <https://doi.org/10.1002/nbm.3517>
23. van Houtum Q, Arteaga de Castro CS, Klomp DWJ, van der Kemp WJM. Full coverage ^{31}P MRSI of the liver with a body coil at 7T. ISMRM 2019. 2019; ISMRM 27th Annual Meeting. <http://cds.ismrm.org/protected/19MPresentations/abstracts/0487.html>
24. Pohmann R, von Kienlin M, Haase A. Theoretical evaluation and comparison of fast chemical shift imaging methods. *J Magn Reson*. 1997;129(2):145-160. <https://doi.org/10.1006/jmre.1997.1245>
25. Clarke WT, Robson MD, Rodgers CT. Bloch-Siegert B_1^+ -mapping for human cardiac (^{31}P) P-MRS at 7 tesla. *Magn Reson Med*. 2016;76(4):1047-1058. <https://doi.org/10.1002/mrm.26005>
26. Raaijmakers AJE, Italiaander M, Voogt IJ, et al. The fractionated dipole antenna: a new antenna for body imaging at 7 tesla. *Magn Reson Med*. 2016;75(3):1366-1374. <https://doi.org/10.1002/mrm.25596>
27. Rodgers CT, Robson MD. Receive array magnetic resonance spectroscopy: whitened singular value decomposition (WSVD) gives optimal Bayesian solution. *Magn Reson Med*. 2010;63(4):881-891. <https://doi.org/10.1002/mrm.22230>
28. Valkovič L, Dragonu I, Almujaayaz S, et al. Using a whole-body ^{31}P birdcage transmit coil and 16-element receive array for human cardiac metabolic imaging at 7T. *PLoS ONE*. 2017;12(10):e0187153. <https://doi.org/10.1371/journal.pone.0187153>
29. Roy K, Wu Y, Meitzler JL, et al. NADPH oxidases and cancer. *Clin Sci*. 2015;128(12):863-875. <https://doi.org/10.1042/CS20140542>
30. Andersen M, Hanson LG, Madsen KH, et al. Measuring motion-induced B_0 -fluctuations in the brain using field probes. *Magn Reson Med*. 2016;75(5):2020-2030. <https://doi.org/10.1002/mrm.25802>
31. van den Wildenberg L, van Houtum Q, van der Kemp WJM, et al. B_0 Shimming of the liver using a local array of shim coils in the presence of respiratory motion at 7T. ISMRM 2019. 2019; #0221 ISMRM 27th Annual Meeting & Exhibition. <https://cds.ismrm.org/protected/19MPresentations/abstracts/0221.html>
32. Boer VO, van de Bank BL, van Vliet G, Luijten PR, Klomp DWJ. Direct B_0 field monitoring and real-time B_0 field updating in the human breast at 7 tesla. *Magn Reson Med*. 2012;67(2):586-591. <https://doi.org/10.1002/mrm.23272>

How to cite this article: van Houtum Q(Q), Mohamed Hoesein F(FAA), Verhoeff J(JJC), et al. Feasibility of ^{31}P spectroscopic imaging at 7 T in lung carcinoma patients. *NMR in Biomedicine*. 2021;34:e4204. <https://doi.org/10.1002/nbm.4204>